Light Metals 2012 *Edited by: Carlos E. Suarez*
TMS (The Minerals, Metals & Materials Society), 2012

Impurity Elements in Raw Gas Ultra-Fines from Aluminium Electrolysis Cells

Heiko Gaertner[1], Arne Petter Ratvik[1], Thor Anders Aarhaug[2]
[1]NTNU, Department of Materials Science and Engineering, NO-7491 Trondheim, Norway
[2]SINTEF Materials and Chemistry, NO-7465 Trondheim, Norway

Keywords: Off-gas, Particulates, Fluorides, Emissions, Ultra-fines

Abstract

The effect of alumina feeding and pot suction rate on the amount and composition of fine particles in raw gases has been investigated. Particle size distribution of ultra-fines (Di < 10 µm) were measured in real time and the chemical composition of particle size groups were analyzed. Mass distribution of dust in fumes from cells under different operational condition were calculated from density estimates based on measured currents which again were converted to particle number impacts and compared to weighted samples. EDS analysis and HR ICP-MS revealed a significant increase in contaminant level for particles with a Di > 0.75 µm. The findings indicate that particles with Di < 1.2 µm consist mainly of quenched bath fumes, $NaAlF_4$, $Na_5Al_3F_{14}$, partly converted to Na_3AlF_6 and Al_2O_3. Particles with Di > 1.2 µm exhibit significant levels of contaminants, presumably entrained particles from the combustion of anode carbon and alumina feed.

Introduction

Aluminium metal quality and current efficiency in electro-winning can be improved by removing contaminants from the raw material feedstock. Removal of the very fine fraction of the fluoride enriched secondary alumina with particle sizes below 45 µm, called "stripping" is a viable method to improve metal quality and cell performance as demonstrated by several authors [1, 2, 3, 4]. Mapping of impurity distribution in the alumina fines and ultra-fines is of interest to develop economical efficient strategy for removal of contaminants, to improve the understanding of scaling and to improve overall process economics. In a previous work, impurity distribution within the ultra-fine fraction of secondary alumina (screen sizes 125, 90, 63, 45, 32 µm and tray) was analyzed [5]. The total impurity level in the secondary alumina increased significantly with decreasing particle diameter. In the present work, raw gases from electrolysis cells were sampled, size classified and analyzed in order to map particle and impurity distribution under different operational conditions. Quantification of gaseous and particulate fluorides is challenging since the relative amount is dependent on sampling and analytical procedures [6]. Fluoride containing particles may undergo hydrolysis and gaseous hydrogen fluoride can adsorb on particles. The objective of this work is to identify characteristic properties of the ultra-fine fractions in raw gases from electrolysis cells under different operational conditions.

Experimental

An Electrical Low Pressure Impactor (ELPI) manufactured by Dekati Ltd. was used to sample fumes form electrolysis cells. The measurement instrument consists of three main components: a charger unit, a cascade impactor and multi-channel electrometer [7]. Particles in the sampling gas are charged and led into the impactor. The impactor separates particles into 13 fractions according to their inertia and consequently their aerodynamic diameter. The electrometers measures the collected charges carried by the particles which are deposited on the electrically insulated impactor stages. The ELPI software converts measured charges to number concentrations (counts). The sampling equipment consists of a heated sampling and dilution line (Dekati DAD-100 axial diluter). A cyclone collects the coarse dust particles. The residual fine particles of D_{50} < 10 µm are fed to the impactor at a flow rate of 10 $lmin^{-1}$. Dilution ratios were determined with a ProtIR 204M/C FTIR spectrometer by comparing concentration changes in tracer gas before and after the dilution. The Dekati ELPIvi 4.0 software was used to compute the particle numbers. Measured particle samples under different operational conditions were analyzed as outlined in Table 1. Chemical composition of particle size groups were analyzed by means of SEM/EDS, XRD and ICP-MS.

Table 1: List of notation, experimental condition and analysis. SC: Single cell. CG: Cell group measurement.

Set	Smelter	Current [kA]	Bath temp. [°C]	AlF_3 [%]	Modus	Cell events	XRD	SEM EDS	ICP-MS	Gravi-metric
a	A	312	953	11.1	CG		x	x		x
b	"				SC		x	x		x
0	B	170	952	10.9	SC					
1	"		956	10.5	CG		x	x		x
2	"				CG		x	x		x
3	"		952	10.9	SC			x		x
4	"		-	-	SC	AE, covers closed		x		x
c	D	162	963	8.9 (10.5-11)	CG					
5	"		-	-	SC	AE, covers opened		x		x
d	"		-	-	SC	Anode cover cutting				
6	"				SC	Anode change				x
7	C	225	962	10.4	CG		x	x	x	x
8	E	298	964	11	SC	DPS 3200			x	x
9	"		971	-	SC	DPS 4100			x	x
10	"		971	-	SC	DPS 7000			x	x

Results and Discussion

As shown in Figure 1, computed mass-weights based on current measurements of raw gas from different electrolysis cells gives significantly higher values than the weighed masses for the particle size class with Di > 6.25 µm. The ELPI-software's conversion of measured charge to mass distributions depends on the assumptions made. Since particle charging and size classification are based on different particle size concepts, approximations and assumptions have been made to make the complex undertaking of real-time particle distribution measurements feasible. Impactor stage midpoints have to be converted to corresponding mobility diameter by estimating particle physical properties [7,8]. Calibration and corrective algorithms are based on uniformity with respect to shape factor and particle density for all impactor stages, which may or may not apply. Deviations from the aerosols' assumed physical properties can cause overestimation in ELPI mass results [9].

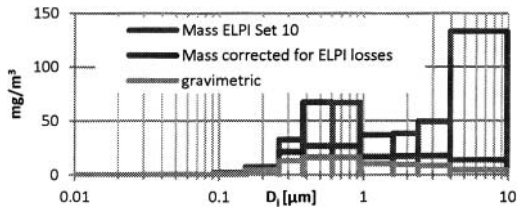

Figure 1: Comparison of mass-concentrations Set 10: Gravimetric (green), corrected for charger losses (red), and as computed by ELPI software based on the assumption of uniform particle density for all particle size classes (blue).

In gravimetric measurements fine particle losses to coarser impactor stages are not critical as the masses are minor [10]. However, when the diffusion charges of fine particles counted on coarser stages are converted from number concentrations to mass, the error may be significant since mass is directly proportional to number count but multiplied by diameter to the power of three. Conversion factors have been calculated to fit the gravimetric measurements with the ELPI measurements. For fumes from aluminium electrolysis cells these correction factors or "effective particle group densities" of the particle size classes D_i are listed in Table 2.

Table 2: Rough estimate of "Effective-particle-group-densities" and corresponding standard deviations. Densities are calculated based on number-concentrations and gravimetric analysis of ten ELPimpactor measurements.

Channel	4	5	6	7	8	9	10	11	12
Stage	3	4	5	6	7	8	9	10	11
Di [µm]	0.12	0.20	0.31	0.48	0.76	1.22	1.95	3.07	6.25
ρ [g/cm³]	2.85	1.11	0.69	0.43	0.42	0.49	0.46	0.42	0.17
Stdev. [g/cm³]	1.26	0.18	0.11	0.13	0.09	0.10	0.11	0.07	0.10
[%]	44	16	16	29	22	21	24	18	60

For particles in the range $0.48 < Di < 3.07$ µm the rough density estimate is 0.44 g/cm³ with standard deviations of 23 %. Due to diffusion losses a significantly lower effective density of 0.17 g/cm³ are calculated for coarse particles with $Di > 3.07$ µm. Unreasonably high densities and large standard deviations are computed for particles with diameter $Di < 0.12$ µm. For the fractions, the very small sample masses close to measurement limits of the micro-balance lead to misinterpretation of the ratio between recorded charges and weight masses (Figure 2).

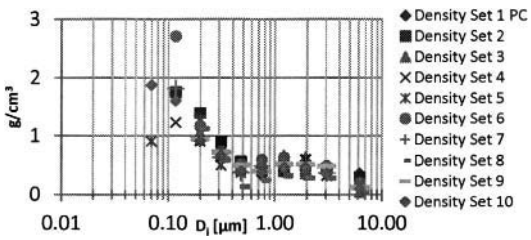

Figure 2: Density correction factors calculated from gravimetrically determined mass-distribution by comparing with measured ELPI- number concentrations.

Assuming that ultra-fines are condensed bath fumes as cryolite, chiolite, sodium tetrafluoroaluminate, aluminium fluoride and sodium fluoride, a density higher than 3 g/cm³ is not reasonable with respect to the origin of the particles [11, 12]. Particle mass concentrations in the raw gases from cell groups of different smelters are shown in Figure 3. With the chosen experimental setup the particle distributions of different cell technologies are similar. This indicates that the particles are mainly vapour condensates as the bath temperatures are close to equal.

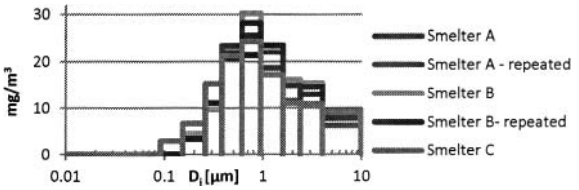

Figure 3: Mass distribution for cell groups calculated from ELPI currents using density estimates from Table 2.

In a subsequent measurement campaign cell fumes were sampled from the conventional duct system at a suction rate of 3980 Nm³ and for comparison from Distributed Point Suction (DPS) system at suction rates of 3200, 4100 and 7000 Nm³/h. The total suction could be split between DPS and conventional suction with varying ratios. Figure 4 indicates that cell fume sampled with DPS are more concentrated since the collection cap which combines feeding and fume capturing is located close to the feeder holes. Thus, collection of cell-fumes is more efficient [13]. Although suction rates were radically changed the variation between recorded mass-concentrations of the different measurements were surprisingly small.

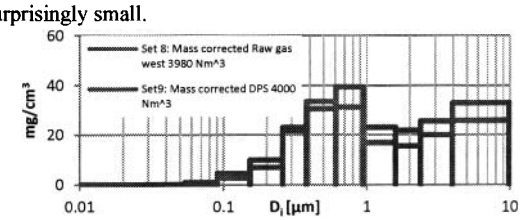

Figure 4: Particle size distribution changes due to DPS-suction. Conventional suction system: 184 mg/cm³, Median 1.02 µm. DPS: 202 mg/cm³, Median 1.12 µm.

The ELPI allows only for online distribution monitoring of a limited measurement range (ultra-fines with $D_i < 10$ µm) which represent only approximately 10-15 % of the total particulate emissions. However, the measurements indicate that a significant increase in DPS suction rate resulted in only minor increase in particle concentrations for the $D_i < 1$ µm. Conversely, fine particle concentrations in the sub-micron range decreased slightly with increasing DPS suction rate, while coarse particle ($D_i > 0.94$ µm) concentrations increases (Figure 5).

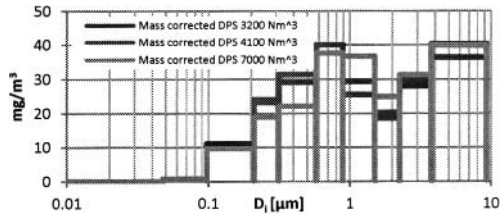

Figure 5: Changes in mass-distribution in fumes sampled from a single cell with DPS-system at different suction rates. Data is computed based on density estimates.

It is assumed that the concentration of bath vapours is dependent on cell operation condition. During the sampling period the evaporation rate is more or less constant. Therefore, it is assumed

that increased suction rate dilutes the bath fumes with surrounding air resulting in a reduction of fines content per Nm^3. On the other hand, coarse particle concentrations increase with increased suction rate since higher flow rates entrain particles with larger aerodynamic diameter into the duct system leading to higher recordings of coarse particles.

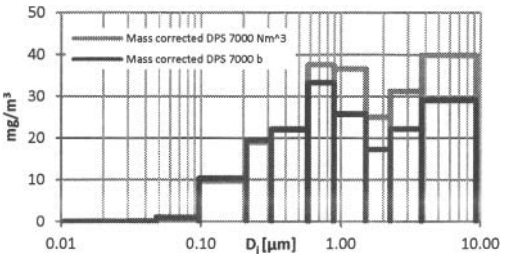

Figure 6: Changes in mass-distribution of a single cell with constant DPS suction rate of 7000 Nm^3 but changes feeding frequency (7.7 sec (green graph) to 18 sec (purple graph).

Increasing the feeding frequency results in an off-set of the mass distribution curve towards the coarser particle sizes. Secondary alumina is typically in a narrow particle size distribution range (D_{90} = 244 µm, D_{50} = 95 µm, D_{10} = 39µm) with a mean particle size between 80-100 µm to minimize segregation and ensure proper handling and dissolution. As shown in Figure 6 the content of coarse particles increases when alumina is more frequently fed to the cell while the ultra-fine particle content $D_i < 0.576$ µm remains more or less unchanged. Although particles with an aerodynamic diameter Di < 10 µm are separated in an aerocyclone prior to the ELPI, the changes in the coarse particle fraction due to entrainment of fine particles in the secondary alumina is obvious.

SEM EDS Results

Examination of secondary electron micrographs of the size classified particulates revealed a change in agglomerate morphology. The structure changes from a needle-shaped fibrous framework with knobbly or grape-like droplets with smaller particulates attached, to spherical droplets, platelets and hexagonally shaped or oblong primary particles.

On substrates with $0.07 \geq Di \geq 0.757$ µm (Figure 7) the agglomerates seem to grow together to a fabric framework and initial agglomerates cannot easily be identified, while individual particles can quite easily be identified on the impactor stages with Di > 1.224 µm (Figure 8). The fibers appear to serve as condensation sites for vapour phases and may partly hydrolyze.

In Figure 9, the EDS results of particles from different impactor stages are plotted in a ternary diagram showing a more homogeneous chemical composition for particles of stages 1 to 8 ($Di \leq 0.757$ µm), while a wider scatter is observed for stages 9-11 with $Di \geq 1.224$ µm (Figure 10).

As the fume originates from cryolite-based melts, the particles consist of chiolite, cryolite droplets and quenched sodium tetrafluoroaluminate (red marks in Figure 9).

The off-set from the expected composition is assumed to be due to a) interaction of the electron beam with several particles and the inaccuracy of EDS analysis method with respect to light elements, b) transformation of multicomponent compositions into ternary diagram data and c) due to decomposition of metastable particles and hydrolysis.

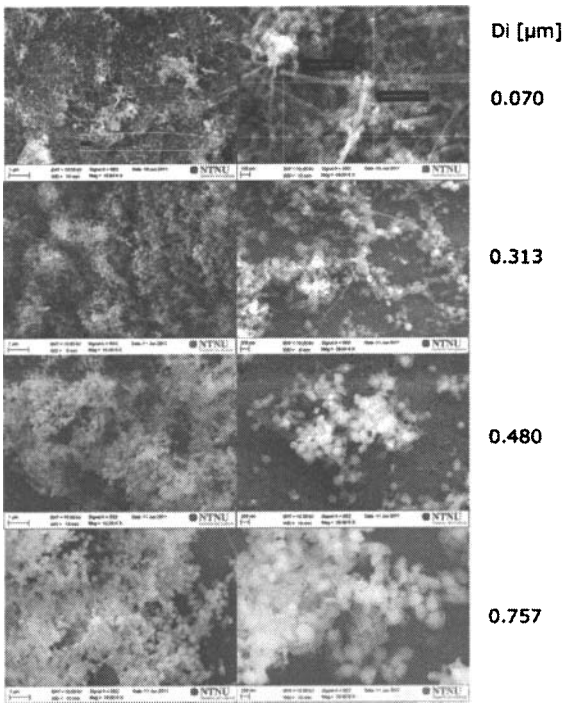

Figure 7: Fabric frame work of and condensate droplets of ultra-fine particles assume to originate from bath vapour phase and entrained bath mist.

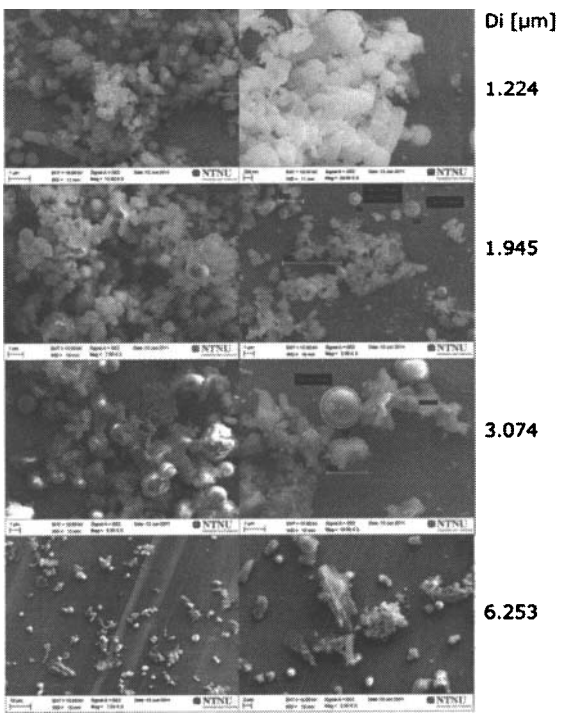

Figure 8: Micrographs of particles assumed to be a mixture of bath fumes with increasing content of entrained particles from alumina feed and anode.

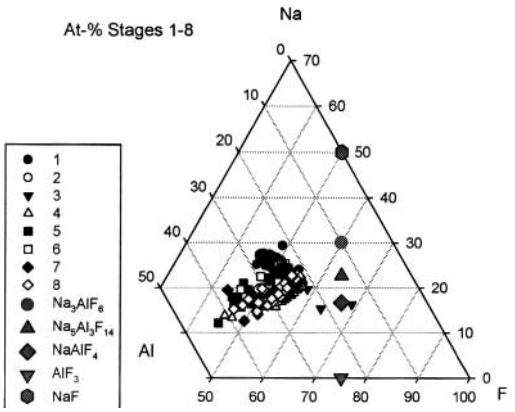

Figure 9: Plot of Energy dispersive spectroscopy data. More or less similar particle composition for the submicron particles of Stages 1-11 was found.

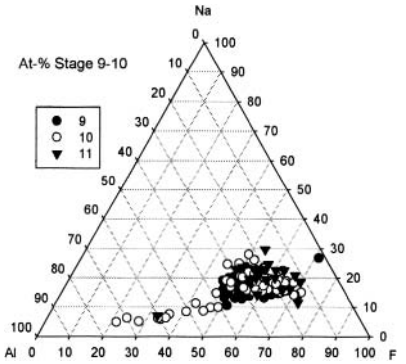

Figure 10 : EDS data plot: More heterogeneous and wider scatter of particle composition for particles with Di > 1 µm. Increasing content of Al_2O_3 was found.

The coarser the particle fraction get the higher is the content of entrained particles from alumina feedstock. EDS analysis revealed that sulfur is more or less present in all samples, while impurities increase significantly for particles with aerodynamic diameters above sub-micron range.
In BSE detector images heavier elements appeared brighter. Ni and Fe containing particles, often accompanied by higher S and P contents, could easily be identified due to their very bright appearance in the back-scatter electron pictures.

XRD
Beside chiolite and corundum, solid sodium tetrafluoroaluminate could be identified with help of XRD analysis. The $NaAlF_4$-pattern became more and more dominant for particles in submicron range as indicated in Figure 11.

ICP-MS
Four sets of size classified particulates were dissolved in acid solution for inductively coupled plasma mass spectroscopy. The instrument sensitivity was significantly reduced due to decomposition of the silver substrates. The disadvantageous Substrate-to-Sample-Mass-Ratio (in average 0.13 mg sample on 132 mg Ag substrate) introduced impurities and led to high background noise which required corrections of ICP-MS results. The small sample masses enhance relative deviations since detected concentrations in the diluted sample solution is related to weight and corresponding weighing uncertainties.

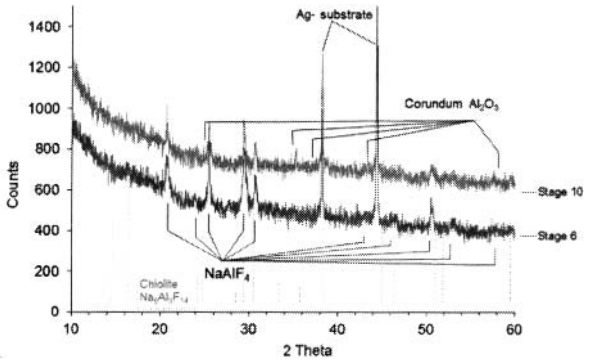

Figure 11: XRD analysis of size classified particles samples Stage 10 Di=1.95. Stage 6 Di= 0.31µm.

However, the ICP-MS analysis confirmed contaminant distribution as previously observed in EDS/SEM analysis. Total impurity content increases with increasing particle size. Potassium exhibits an opposite trend while sulfur shows a peak-concentration at approximately 0.40 µm (Figure 12).

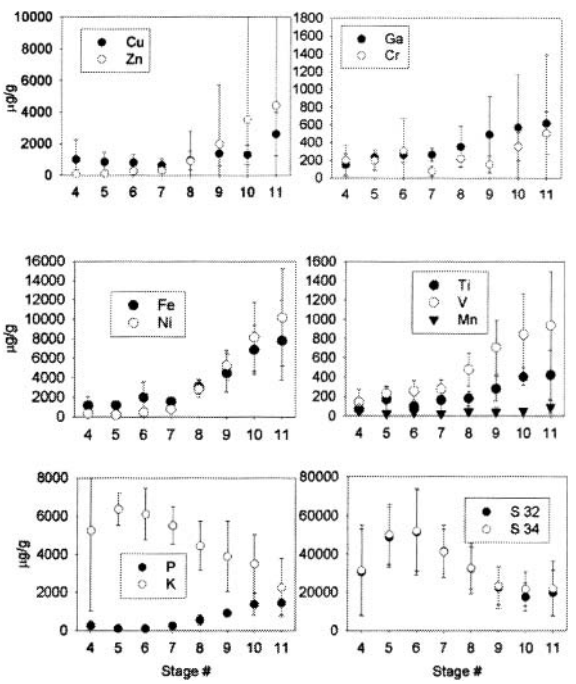

Figure 12: Impurity element distributions in raw-gas particulates.

The submicron fraction exhibits a Na:Al atomic-%-ratio close to that of $NaAlF_4$, while the fraction with aerodynamic diameter $D_i > 1$ µm show a significantly increase in aluminium content. This trend is enhanced for DPS samples as shown in Figure 13.

Important observations during ELPI measurement are summarized in the bullet-point list below.

- Cell group measurements at different smelters give similar particle mass distribution with minor differences in ultra-fine concentrations for particles with $D_i < 10$ µm.

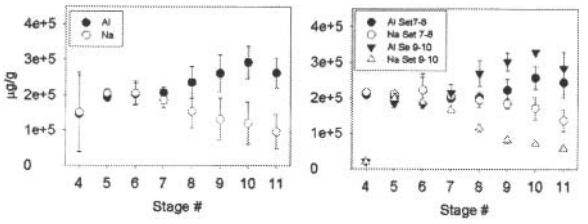

Figure 13 : ICP-MS-results for sodium and aluminium: Atom-% ratio Na:Al = 1.2 : 1 almost constant for Di < 0.76 µm . Di > 1.22 µm Na:Al = 1 : 2.6. Left: Average for all sets. Right: An enhanced trend is observed for DPS samples Set 9 and set 10.

- Changes in suction rate have a relatively small effect on particle distribution for $D_i < 10$ µm. Particle concentrations for fractions with $D_i < 0.6$ µm are reduced when suction rate is increased (while for this particle fraction at constant suction rate, but altered feeding sequence, the particle concentrations remain unchanged).
- Particle concentrations for $D_i > 0.6$ µm increase significantly when more frequent alumina feeding takes place (entrainment).
- Micrographs revealed that particles collected on different impactor stages are of different physical shape and structure. Particles captured on same impactor stage, but originating from different cell types and/or under different operational conditions have similar appearance (morphology).
- Impurity as V, Ti, Fe, Ni , and Mo could not be detected in submicron particles, while the content of contaminants increased significantly in particle size groups with particle sizes Di > 1 µm. More and more inhomogeneous particle composition and morphology is observed with increasing aerodynamic particle diameter.

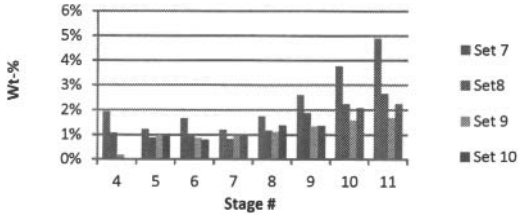

Figure 14: Distribution of impurity elements P, K Ti, V, Cr, Mn, Fe, Ni, Cu, Zn, Ga, and Mo over the particle size range of $0.12 \leq Di \leq 6.25$ µm.

- $NaAlF_4$-pattern was dominant in submicron particle size classes. Noise and peak broadening due to nanoparticles and very small sample masses made detection of impurity compound and quantification impossible.
- ICP-MS results confirm contaminant distribution as observed in EDS SEM analysis, i.e. significant particle composition changes from Stage 8 (Di=1,22 mm) to larger particle diameters (Figure 14). Enhanced trends for DPS samples with respect to main components Na and Al are observed (Figure 13).

Conclusion

It is commonly accepted that the fines particulates in raw gases from electrolysis cells originate from condensation and hydrolysis of the vapour phases, mainly $NaAlF_4$ dissociates into solid chiolite and aluminium fluoride [6]. Coarser particles from alumina feedstock, bath-cover material, electrolyte droplets and remains from incomplete anode carbon consumption are entrained into the raw gases, e.g. by bubble burst due to gas evolution under alumina feeding and CO_2 release as sketched in Figure 15.

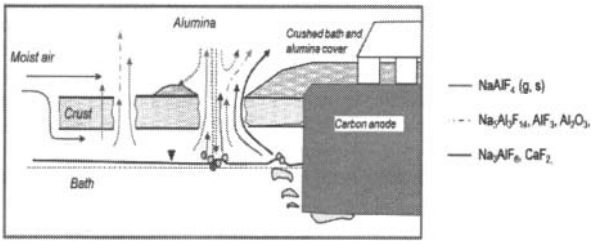

Figure 15: Sketch of particle evolution and entrainment into raw-gases. Quenching and hydrolysis of bath vapours.

The observation of changes in particle distribution, morphology and composition led us to the following conclusions:

i) Submicron particles Di < 1µm are mostly quenched bath fumes, consisting of typical components from cryolite-based melts with a considerable content of $NaAlF_4$ as detected by XRD, EDS and ICP-MS (Na-Al-at-%) and a low content of contaminants. Dilution of these fume components takes place when the suction rate is increased but particle distributions remain more or less unaffected during alumina feeding to the cells. These condensed vapours are a characteristic background cell emission assumed to be mainly dependent on bath evapouration conditions.

ii) An increase in intermediate particle emissions ($Di > 0.6$ µm to 1.2 µm) was observed during alumina feeding, This particle fraction has a low contamination level assumed to be bath mist generated by gas bubble burst of small energy rich bubble introduced into the bath during alumina feeding. Crust breaking and feeding introduces alumina and humidity into the molten salt (the LOI is typically in the range of 0.6 and not higher than 1 %). Moisture from the alumina will evapourate and help to disperse and dissolve the alumina in the bath. The water vapours together with combustion gases and hydrolysis products escape though the

feeder hole with anode gases and carry away vapours, fines from alumina, crust cover material and bath droplets into the fume capturing system. It is assumed that the gas evolution related to alumina feeding (gas and moisture in porosities of smelter grade alumina) introduce energy rich small bubbles in to the bath (high surface energy). When the bubbles burst, bath droplets will entrain into the off gas and expose the fumes to hydrolysis leading to increased fluoride emission in form of gaseous HF and particulate.

iii) Due to the higher contaminant level and varying morphology it is assumed that the coarse particle fraction with Di $\geq$ 1.22 µm is a mixture of dust from alumina and cover material, splashed bath, and entrained particles as sot and residuals from anode consumption.

The ELPI is a useful tool to monitor variations in the ultra-fine fraction (Di < 10 µm) over time. Operational changes and their influence on particle number-concentration can be linked to particulate emissions since relative changes in number concentrations are easily detected. The performed measurements show that it is possible to determine the effect of the cleaning cycle and to monitor the condition of the filter bags as well as the particulate emissions due to alumina feeding. The quality of real-time measurement data need to be improved with respect to weight distribution. The current adjustment of EPLI measurement to give a better fit with weight distributions is a very rough approximation based on industrial measurements with a high variance. Diffusion losses are significant for Stages 11 and 12 leading to considerable overestimation of numbers of particles. Further investigations of the physical properties of the complex agglomerates are needed for better predictions of particle weights from current measurements.

Further work

The analysis of ultra-fine particle emissions from electrolysis cells presents a good basis for understanding the particle composition of the fumes from an electrolysis cells. A study of the impurity distribution in secondary alumina[5] revealed that impurity loading increases with decreasing particle diameter with total impurity element concentrations of approx. 3 % for the fraction -32 µm, while the recent work indicate that the impurity level in the fumes increases with particle diameter larger than 1µm. Further work should look at the impurity distribution in the fraction 1 µm < Di < 32 µm of both fumes and alumina feedstock to give a more complete picture of contaminant distribution in the different fractions.

Acknowledgment

This study is a part of the ROMA research project with financial support of the Research Council of Norway and the Norwegian aluminium and metallurgical industry. An essential part of this research is conducted during measurement campaigns at industrial cells and the support of staff and operators at the plants are highly appreciated.

References

[1] E. Cutshall, "Removal of phosphorus from dry scrubber alumina," Light Metals, pp. 927-933, (1979).

[2] P. Lossius and H. Bye, "Removing impurities from secondary alumina fines", Light Metals, pp. 249-258, (1992).

[3] L. Schuh and G. Wedde, "Removal of impurities from dry scrubbed fluoride enriched alumina", Light Metals, pp. 399-403, (1996).

[4] E. Sturm and G. Wedde, "Removing impurities from the aluminium electrolysis process", Light Metals, pp. 235-240, (1998).

[5] T. A. Aarhaug and A. P. Ratvik, "Sintef report: Secondary alumina and anode cover material characterization", ROMA activities 2008-2009, Project No.: 80524021 (2010-07-09).

[6] J. Thonstad, P. Fellner, G. M. Haarberg, J. Hives, H. Kvande and A. Sterten, "Aluminium electrolysis", 3rd edition, Aluminium Verlag, ISBN 3-87017-270-3, (2001).

[7] K. P. J. Keskinen and M. Lehtimki, "Electrical low pressure impactor", J. Aerosol Sci.,vol. 23, no. 4, pp. 353-360, (1992).

[8] M. Moisio, "Real time size distribution measurement of combustion aerosols", Publications 279, Tampere University of Technology (Tampereen Teknillinen Korkeakoulu), (1999), ISBN 952-15-0328-9, ISSN 0356-4940.

[9] D. L. Hei, "Unidealities in ELPI mass measurements", Dekati Ltd. Technical Note, modified 2007.

[10] A. Virtanen, M. Marjamki, J. Ristimki, and J. Ksekinen, "Fine particle losses in electrical low pressure impactor", Journal of Aerosol Science, vol. 32, pp. 389-401, (2001).

[11] J.W. Anthony, R.A. Bideaux K.W. Bladh and M.C. Nichols, "Handbook of Mineralogy", Mineralogical Society of America, Chantilly, VA 20151-1110, USA., http://www.handbookofmineralogy.org/

[12] M. Bruno, O. Herstad, and J. Holm, "Stability and structure of sodium tetrafluoroaluminate $NaAlF_4$, ICDD-Pattern-nr. 00-051-1675", Acta Chem. Scand., vol. 52, pp. 1399-1401, (1998).

[13] O.-A. Lorentsen, A. Dyrøy and M. Karlsen, "Handling CO2EQ from an aluminium electrolysis cell", Light Metals, pp. 263-268, (2009).